Generation of high-energy electron-positron pairs in the collision of a laser-accelerated electron beam with a multipetawatt laser

M. Lobet,[1,2,*] X. Davoine,[1,†] E. d'Humières,[2] and L. Gremillet[1,‡]

[1]*CEA, DAM, DIF, F-91297 Arpajon, France*
[2]*CELIA, UMR 5107, Université de Bordeaux-CNRS-CEA, 33405 Talence, France*

(Received 15 October 2016; published 3 April 2017)

Generation of electron-positron pairs via the multiphoton Breit-Wheeler process in an all-optical scheme will be made possible on forthcoming high-power laser facilities through the collision of wakefield-accelerated GeV electrons with a counter-propagating laser pulse of 10^{22}–10^{23} W cm^{-2} peak intensity. By means of integrated 3D particle-in-cell simulations, we show that the production of high-density sources of ultrarelativistic electron-positron pairs is within the reach of soon-to-be-available laser systems. Under physical conditions accessible to the dual-beam CILEX-Apollon facility, we find that the generated positrons can carry a total charge of 0.05–1 nC, with a mean energy of 100–400 MeV and an angular divergence of 0.01–0.1 rad. The variations of the positron source's properties with respect to the laser parameters are also examined.

DOI: 10.1103/PhysRevAccelBeams.20.043401

I. INTRODUCTION

The generation of dense electron-positron (e^-e^+) pair beams or plasmas is of great interest in many research areas, encompassing fundamental science [1], accelerator physics [2], material analysis [3], and laboratory astrophysics [4]. In the latter field, a driving goal is to understand the formation and dynamics of the pair plasmas involved in a variety of powerful space environments (pulsar winds, gamma-ray bursts, active galactic nuclei) [5]. The laboratory reproduction of these phenomena is nonetheless hampered by the need to create pair plasmas dense enough to trigger collective effects. The use of ultraintense, short-pulse lasers provides a promising path to this objective, as testified by the various schemes put forward in recent years [6–12]. The experimental studies carried out so far exclusively relied on pair creation mechanisms induced by relativistic electrons in atomic Coulomb fields. The positrons were generated in thick (∼cm) high-Z solids through either a two-step process, where a bremsstrahlung photon emitted by an electron subsequently converts into an electron-positron pair via the Bethe-Heitler process [13], or the one-step Trident process [14,15], where pair creation is mediated by a virtual photon. Such energetic electrons were produced either by direct irradiation of the convertor target by an

intense ($\sim 10^{20}$ W cm^{-2}) picosecond laser [6] or by a few-femtosecond laser wakefield accelerator [7], in both cases leading to record positron densities of $\sim 10^{16}$ cm^{-2}.

The coming into operation of multi-PW lasers (e.g., the CILEX-Apollon [16] and ELI [17] facilities), expected to reach $\sim 10^{23}$ W cm^{-2} intensities, should make it possible to investigate alternative concepts of pair generation based on quantum electrodynamic (QED) effects [9,18]. Most notable among these is the multiphoton Breit-Wheeler process, in which γ-rays, produced via nonlinear inverse Compton scattering of laser photons by relativistic electrons, decay in turn into electron-positron pairs [19,20]. Theory and simulations predict that quasineutral, high-density ($> 10^{21}$ cm^{-2}) relativistic pair plasmas could be generated from thin solid foils [21], near-critical plasmas [22], gas jets [23] or through pair cascading from seed electrons or photons [10,24–26]. Electron-positron pair production may be also possible in the framework of the flying-mirror concept, as presented in [27]. These promising laser-based scenarios have prompted advanced theoretical developments of the Breit-Wheeler process, e.g., allowing for pulsed or modulated laser fields [28–32].

In the near future, however, the most accessible route to laser-driven pair production via the multiphoton Breit-Wheeler process will exploit the collision of relativistic electrons with counter-propagating high-power laser pulses [33–35]. This concept was demonstrated two decades ago at SLAC by making a 46-GeV electron beam interact with a 10^{18} W cm^{-2} laser [36], and may be reproduced at higher electron energies on the future linear collider [37]. An all-optical scheme, based on a laser wakefield accelerator (LWFA) instead of a conventional accelerator, should be within the reach of multi-PW, multibeam laser systems as schematically described in Fig. 1. Recent state-of-the-art

---

[*]mathieu.lobet@cea.fr
[†]xavier.davoine@cea.fr
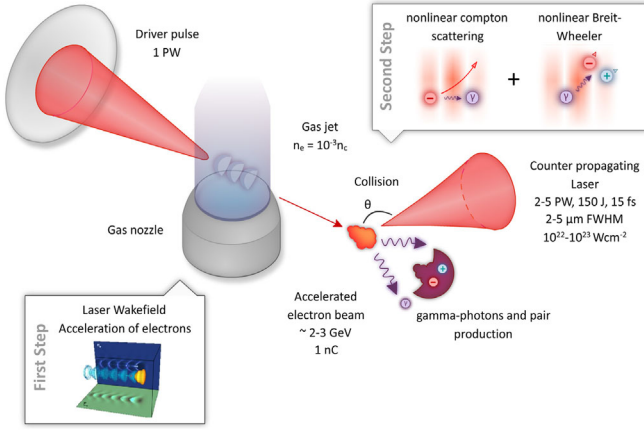[‡]laurent.gremillet@cea.fr

FIG. 1.   All-optical setup for e^-e^+ pair generation. First step: a multi-GeV electron beam is created in a laser wakefield accelerator. Second step: the electron beam collides head-on with an ultraintense, short-pulse laser pulse, leading to strong-field quantum electrodynamic emission of γ-ray photons, which in turn decay into e^-e^+ pairs.

experiments have confirmed the potential of this all-optical configuration for generating high-brilliance γ-ray photon beams [38], consistent with numerical and model predictions [39–43].

In order to provide guidelines for future experiments, we present in this paper the first integrated, one-to-one simulation study of pair production from laser-electron beam collisions in upcoming multi-PW laser facilities. Focusing on interaction conditions accessible to the dual-beam CILEX-Apollon system [16], we characterize in detail the generated e^-e^+ beam and examine the sensitivity of its properties to the laser parameters. This paper is organized as follows. In Sec. II, we estimate the γ-ray and positron yield in a broad parameter range using a reduced kinetic model. In Sec. III, we present typical results of our integrated particle-in-cell (PIC) simulation framework, which combines the quasicylindrical code CALDER-CIRC and the three-dimensional (3D) code CALDER. In Sec. III A, so as to optimize the pair-creation efficiency of the electron source, we consider a LWFA scheme based on a two-step plasma profile, from which we predict electron beam energies in excess of 3 GeV. Then, in Sec. III B, we describe in detail the ultrafast dynamics of the γ-ray and positron generation during the collision of the high-energy electron beam with a 10^{23} W cm^{-2}, 15 fs laser pulse. The dependencies of the γ-rays' and positrons' properties (mean energy, yield, divergence) with respect to the laser parameters are addressed in Sec. III C. Finally, the modifications brought by a non-collinear interaction geometry are examined in Sec. III D.

II. THEORETICAL ESTIMATES OF PAIR PRODUCTION

We start by estimating the efficiency of pair production during the collision of a relativistic electron beam with an

intense laser by means of a reduced kinetic QED model [34,44,45]. This model describes the time evolution of the electron, positron and photon energy distributions under the action of a counter-propagating laser plane wave (propagating along the x-axis and polarized along the y-axis), taking into account nonlinear inverse Compton scattering and the multiphoton Breit-Wheeler process. Unidirectional propagation of the particles at the speed of light is assumed, while advection and collective effects are neglected. In the general noncollinear case [see Fig. 2(d)], the geometry of the laser-electron interaction is characterized by the angles $\theta = -\arctan\left(p_z/p_x\right)$ and $\varphi = \arctan\left(p_y/\sqrt{p_x^2 + p_z^2}\right)$, where $\mathbf{p}$ is the electron momentum (assumed constant). As is well-known [18,46], the efficiency of the photon and pair production in an instantaneous electromagnetic field $(\mathbf{E}, \mathbf{B})$ is determined by the strength of the electron quantum number

$$\chi_- = \frac{\gamma_-}{E_s}\sqrt{(\beta_- \cdot \mathbf{E})^2 - (\mathbf{E} + \mathbf{v}_- \times \mathbf{B})^2}, \qquad (1)$$

and of the photon quantum number

$$\chi_\gamma = \frac{\gamma_\gamma}{E_s}\|\mathbf{E}_\perp + c\mathbf{n} \times \mathbf{B}\|, \qquad (2)$$

where γ_- is the electron Lorentz factor, $\mathbf{v}_-$ the electron velocity, $\beta_- = v_-/c$, $\gamma_\gamma = \varepsilon_\gamma/m_e c^2$ the normalized photon energy (m_e is the electron mass), $\mathbf{n}$ the unit vector along the
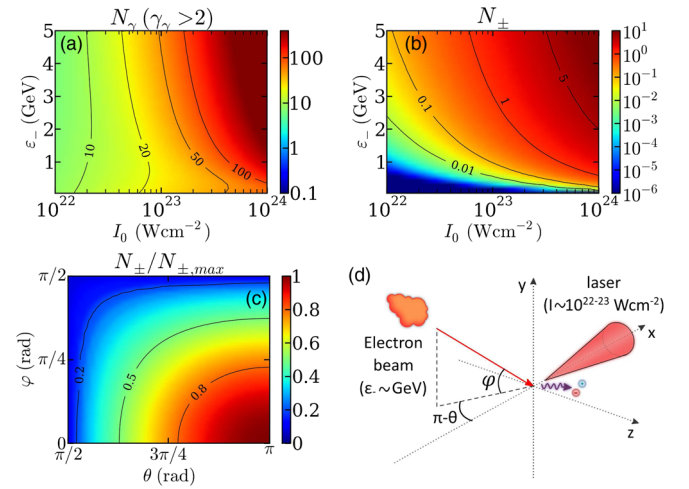

FIG. 2.   Reduced kinetic-QED modeling: (a) Number of γ-ray photons of energies $\varepsilon_\gamma > 2m_e c^2$, N_γ, and (b) of e^-e^+ pairs, $N_\pm$, produced during the entire laser interaction in the head-on collision of an electron with a laser plane wave (Gaussian temporal profile of 15-fs FWHM duration), as a function of the electron energy and laser intensity. (c) Ratio of the pair yield in an oblique collision over the pair yield in a head-on collision, $N_{\pm,\max}$, as a function of the angles θ and φ. Contour lines are shown as black curves in (a), (b), and (c). (d) Schematic of the electron-laser collision geometry.

photon direction, $\mathbf{E}_\perp$ the electric field component normal to **n**, and $E_s = m_e^2 c^3/e\hbar \simeq 1.3 \times 10^{18}$ V/m the Schwinger field [46]. Within our simplified description, the effect of oblique incidence is to reduce both χ_- and χ_γ, and thus modify the associated inverse Compton scattering and multiphoton Breit-Wheeler cross sections [18,46].

In the case of a head-on collision ($\theta = \pi$, $\varphi = 0$), Figs. 2(a,b) display, as a function of the laser intensity ($10^{22} \leq I_0 \leq 10^{24}$ W cm^{-2}) and the electron beam energy ($0.1 \leq \varepsilon_- \leq 5$ MeV), the predicted number of photons of energies $\varepsilon_\gamma > 2 m_e c^2$ (N_γ) and positrons ($N_\pm$) created per beam electron during the whole laser interaction. In the parameter range considered, the photon yield proves mainly sensitive to the laser intensity, with strong γ-ray emission ($N_\gamma \geq 10$) setting in for $I_0 \gtrsim 2 \times 10^{22}$ W cm^{-2}. By contrast, pair production appears to depend on both I_0 and ε_-, significant positron yield ($N_\pm = 0.1$) being achieved for either a 5-GeV electron interacting with a 10^{22} W cm^{-2} laser wave, or a $\sim$0.5-GeV electron in a 10^{24} W cm^{-2} wave.

Assuming a LWFA driven by the 1-PW laser pulse of the CILEX-Apollon system (0.8-μm wavelength, 15-J energy, 30-fs FWHM duration, 23-μm FWHM spot size), we expect from Lu's model [47] a typical beam energy of $\sim$2 GeV for a total charge of $\sim$1 nC. This beam is then made to collide with the CILEX-Apollon 5-PW, 15-fs laser pulse, focused to a maximum intensity of 10^{23} W cm^{-2}. For a head-on collision under such conditions, an electron is expected to produce approximately 20 γ-ray photons and 0.5 $e^- e^+$ pair during the laser interaction [Fig. 2(b)]. This will yield a positron distribution with a total charge close to that of the incident electron beam, and with an average energy of several hundred MeV (not shown), comparable with the average photon energy.

The reduction in the positron yield at oblique incidence is quantified in Fig. 2(c), where the positron yield (normalized to that for a head-on collision) is plotted against the angles (θ, φ). Here, the electron energy and laser intensity are set to $\varepsilon_- = 2$ GeV and $I_0 = 10^{23}$ W cm^{-2}, and the laser propagation is kept unchanged in the $-x$ direction. The positron yield exhibits relatively weak variations when increasing the incidence angle: it drops by a mere factor of $\sim$2 for $\theta = 110°$ (or $\varphi = 70°$) and by a factor of 10 for $\theta = 90°$ (or $\varphi = 90°$).

III. INTEGRATED KINETIC SIMULATIONS

For a more accurate description of pair production, we make use of two complementary particle-in-cell (PIC) codes. The laser wakefield acceleration is simulated by means of the code CALDER-CIRC [48], based on a quasi-cylindrical discretization of the Maxwell equations, which allows one to handle the spatio-temporal scales of the problem at a reduced computational cost. The resulting electron beam is then transferred to the 3D Cartesian code

CALDER [49], enriched with Monte Carlo models of the photon and pair production [45].

A. Electron acceleration with the Apollon 1-PW laser

In a first stage, we simulate the wakefield acceleration induced by the Apollon 1-PW laser (the parameters of which are given above). We first consider a 1.5-cm-long, flat plasma profile with a density of $1.6 \times 10^{-3} n_c$ (n_c is the critical density at 1 μm). In good agreement with Lu's scaling laws [47], we obtain a 2-GeV electron bunch accompanied by a broad low-energy tail, with a total beam charge of 5 nC. This can be seen in the space-resolved electron energy spectrum displayed in Fig. 3(a).

In order to boost the beam energy, which is a key parameter for efficient pair creation, we resort to a two-step plasma profile, comprising a 6.3-mm-long plateau at $1.6 \times 10^{-3} n_c$ followed by a 5.6-mm-long plateau at $3.2 \times 10^{-3} n_c$. This density jump aims at shortening the plasma bubble when the trapped electrons approach their dephasing length, hence relocating them in the highest accelerating region of the wakefield, at the back of the bubble. This selects the beam head, increasing its energy up to $\sim$3 GeV, while reducing its charge to $\sim$2 nC. The increased monochromaticity of the whole electron beam (above 100 MeV) is demonstrated by the space-resolved energy spectrum of Fig. 3(b) and the final energy spectrum of Fig. 3(c). From the 3D space-energy distribution shown in Fig. 3(d), it is found that 63% of the total beam charge is contained in the beam head (between 2.5 and 3.8 GeV), while the rest is mostly carried by a secondary electron bunch (with energies under
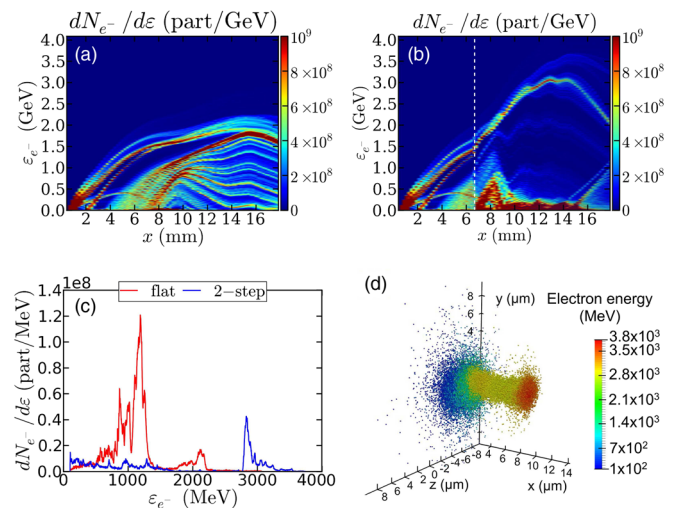

FIG. 3. Electron energy spectrum as a function of the longitudinal position in the plasma for the flat (a) and two-step (b) plasma density profiles. In (b), the dashed white line indicates the location of the density jump. (c) Energy spectra of the beam electrons for the flat (red) and two-step (blue) density profiles. (d) 3D space-energy distribution of the beam electrons for the two-step density profile. Each dot corresponds to a macroparticle, colored as a function of its energy in MeV (see color map).

1.7 GeV) resulting from self-injection in the shortened bubble. The beam has an average divergence of ~3 mrad, transverse FWHM sizes of ~4 μm and ~2 μm FWHM, respectively along and normal to the laser polarization direction (y-axis), and a longitudinal length of ~12 μm.

B. Pair generation during the collision with the Apollon 5-PW laser

The electron beam is then made to collide head-on with the CILEX-Apollon 5-PW laser. The pulse parameters (15-fs duration, 2-μm focal spot) are chosen so as to reach a maximum intensity of 10^{23} W cm^{-2} at the beam head. Consistently with the previous simple estimates, the laser-beam interaction is strong enough to cause copious photon and pair production, as depicted in Figs. 4(a,b) (see also movie in Supplemental Material) [50]. Furthermore, Fig. 4(b) shows that pair production is maximal at the beam head where the tightly-focused pulse encounters the most energetic electrons. The e^-e^+ pairs carry ~5% of the incident electron beam energy, with a total positron charge $Q_+ \sim 0.8$ nC amounting to ~38% of the initial beam charge. As predicted by the reduced QED model, the pulse intensity is too low to achieve global quasineutrality, i.e., the production of more than an e^-e^+ pair per incident electron.

At the end of the interaction, however, most of the incident electrons have been expelled by the laser out of the central pair-filled region [Fig. 4(c)], so that the local positron density ($n_+ \sim 0.13 n_c$, averaged over a 2-μm transverse width at the beam head) makes up a significant fraction (~40%) of the total leptonic density, $n_- + n_+ \sim 0.32 n_c$.

The photon and pair generation dynamics is detailed in Figs. 5(a–d), Figs. 6(a–d), and Figs. 7(a–d), which represent, respectively, the space-energy phase spaces of the primary beam electrons, generated photons and positrons at successive times during the laser interaction. Radiative losses become strong when the electron quantum parameter attains values $\chi_- \gtrsim 0.1$ [18]. For electron energies of ~1−2 GeV, this quantum radiation reaction regime is achieved as soon as the electrons experience a laser intensity $\gtrsim 10^{21}$ W cm^{-2} [see Fig. 5(b)]. As a consequence, the beam head's electrons have lost more than 90% of their initial energy by the time they see the laser maximum [Fig. 5(c)]. During the collision, 85% of the beam energy is radiated in the form of a broad photon distribution, as is seen in Fig. 6(d). At their creation time, the energy spectrum of the photons [Fig. 8, dashed green line] extends from hard x-rays to γ-rays, with an average energy of 33 MeV and a maximum energy of 3.5 GeV, close to the
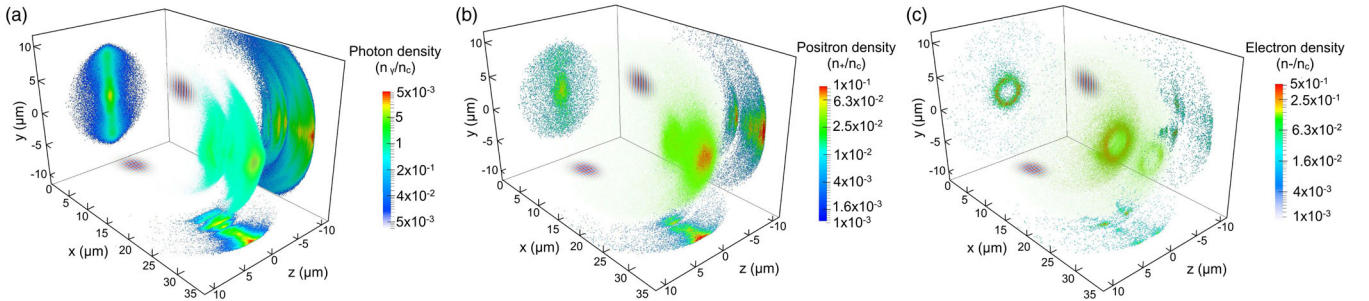

FIG. 4. 3D density distributions of the photons (a) positrons (b) and electrons (both from the primary beam and the nonlinear Breit-Wheeler process) (c) at the end of the laser interaction. Density slices along the $x = 27.5$ μm (corresponding to the densest part of the beam head), $y = 0$ and $z = 0$ planes are projected onto the yz, xz and xy domain boundaries, respectively. The leftward-moving laser pulse is visualized by its normalized electric field, $eE_y/m_e c \omega_0$, projected on the domain boundaries (blue and red colors near $x = 5$ μm). Animations of these density distributions can be watched in the Supplemental Material [50].

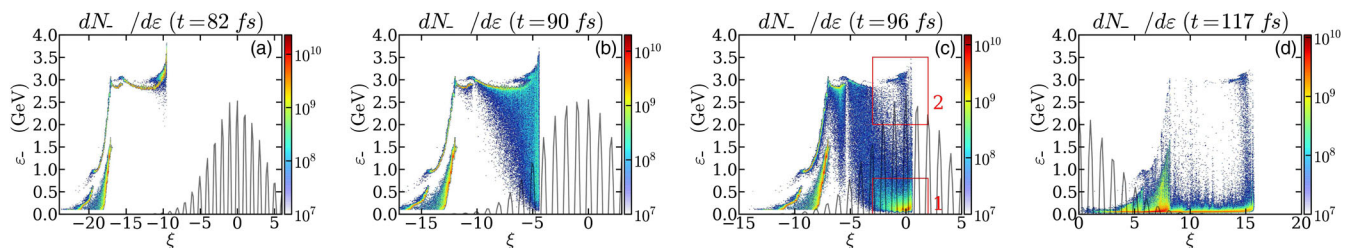FIG. 5. Electron energy spectra (transversely integrated, in particles per GeV) before ($t = 82$ fs) (a), during ($t = 90$ fs and $t = 96$ fs) (b,c) and after ($t = 117$ fs) (d) the laser-beam collision, as a function of the relative distance $\xi = [x - x_p(t)]/\lambda_0$ to the laser maximum x_p (λ_0 being the laser wavelength). In panel (c), the red frame 1 locates the on-axis beam head after strong radiative deceleration in the rising part of the laser, while the red frame 2 encloses weakly-interacting beam electrons, traveling sideways from the laser focal spot. In panels (a-d), the gray line plots (in arbitrary units) the on-axis laser field E_y.
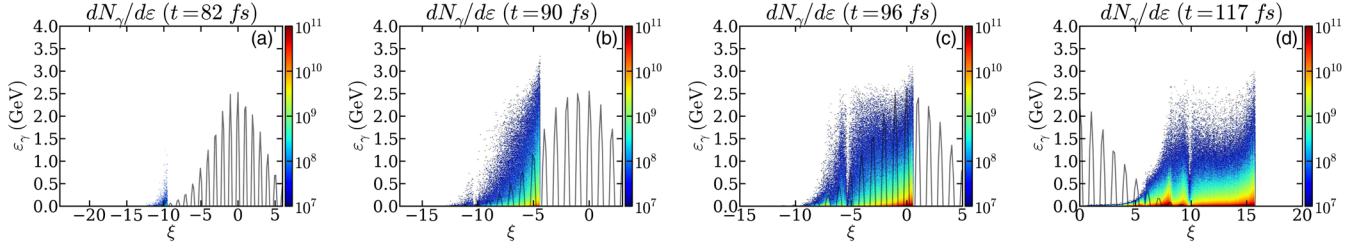
FIG. 6. Photon energy spectra (transversely integrated, in photons per GeV) before (a), during (b,c) and after (d) the laser-beam collision, as a function of the relative distance $\xi = [x - x_p(t)]/\lambda_0$ to the laser intensity peak position x_p (λ_0 being the laser wavelength).
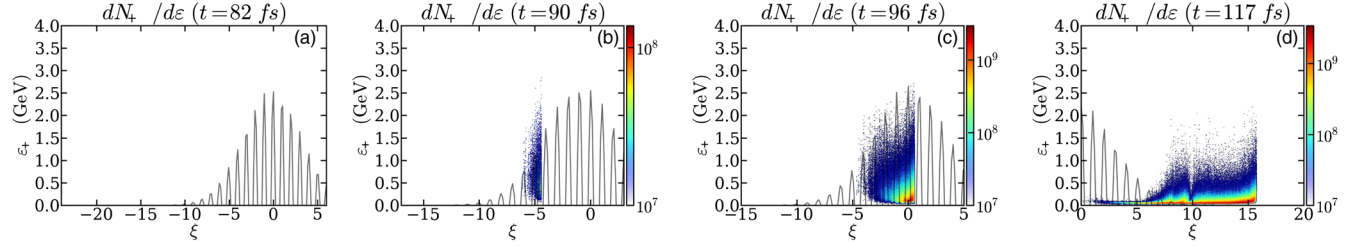

FIG. 7. Positron energy spectra (transversely integrated, in particles per GeV) before (a), during (b,c) and after (d) the laser-beam collision, as a function of the relative distance $\xi = [x - x_p(t)]/\lambda_0$ to the laser intensity peak position x_p (λ_0 being the laser wavelength).

maximum electron energy. Around their average energy, the forward-directed photons present an angular divergence of ~3 mrad, equal to the beam's. The brilliance is computed at the average photon energy from the angle-energy distribution $d^2N_\gamma/d\epsilon d\theta_x$, where $\theta_x = \arctan(k_\perp/k_x)$, k_x is the longitudinal photon wave vector and $k_\perp = \sqrt{k_y^2 + k_z^2}$ is the transverse one. Approximating the emission surface to the electron beam radius yields an approximate brilliance of ~5×10^{23} photon ss^{-1} mm^{-2} mrad^{-2} 0.1% BW, three orders of magnitude larger than the current experimental record in laser-based Compton sources [38].

Following the interaction, the electron beam spectrum is strongly broadened towards lower energies, with a final average energy of ~190 MeV [Fig. 8, solid red curve]. The relatively large value of the maximum energy (~3.2 GeV) corresponds to off-axis electrons weakly interacting with
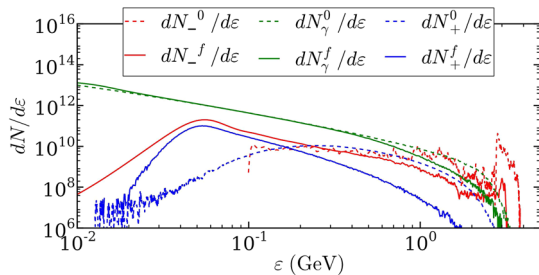

FIG. 8. Integrated energy spectra (in particles per GeV) of the electrons (red), photons (green) and positrons (blue). The solid lines ($dN^f/d\epsilon$) correspond to the final spectra; the dashed lines ($dN^0/d\epsilon$) plot the electron beam spectrum before the laser interaction, and the photon and positron spectra at birth time.

the tightly-focused laser field. This maximum energy is found to drop to 1.5 GeV for a laser plane wave of the same intensity and duration (not shown).

From comparison of the photon spectra at birth and after the collision [Fig. 8, green curves], we find that pair production mainly arises from photons of energy $\gtrsim 0.5$ GeV. These photons have a decay length close to the pulse length, and they are produced in large numbers only during a few periods before the intensity peak [Fig. 6(c)].

The e^-e^+ pairs are created with a broad energy distribution (from ~10 MeV to 3 GeV), associated with an average value ~0.5 GeV [see Fig. 7(d) and Fig. 8, dashed blue curve]. However, while subsequently moving through the remaining part of the pulse, these particles undergo significant radiative losses [compare Figs. 7(c) and (d)] and the emitted photons can in turn trigger a short-duration pair cascade. At the end of the interaction, about 4.5% of the total positron number originates from cascading, while the positron spectrum is strongly shifted to the low-energy side, with a much reduced mean energy ~110 MeV [Fig. 8, solid blue curve].

The final angular spread of the positrons ($\theta^f_{+,xy} \sim 0.33$ rad and $\theta^f_{+,xz} \sim 0.2$ rad in the laser polarization and perpendicular planes, respectively) exceeds by two orders of magnitude that of the incident electrons (~0.003 rad), and is also significantly larger than the angular spread of the positrons at birth ($\theta^0_{+,xy} \sim 0.014$ rad and $\theta^0_{+,xz} \sim 0.001$ rad). Moreover, it appears to be close to the final divergence of the electron beam ($\theta_{-,xy} \sim \theta_{-,xz} \sim 0.3$ rad). As for the electrons, the increase in the positron angular

spread during the laser interaction has two possible origins. First, in the quantum radiation reaction regime considered here, photon emission in the laser field goes along with strong angular scattering, even in the plane-wave case [51]. This deflection mainly takes place in the xy laser polarization plane. As time increases, the radiating particles progressively lose x-momentum while their y-momentum saturates at a value $p_y \propto a_0$ after a few laser cycle [51,52] where $a_0 = eA_0/m_e c$ is the normalized laser potential amplitude with A_0 being the laser amplitude. This feature starkly contrasts with classical radiation reaction, through which a particle cannot gain transverse momentum from a plane wave.

In order to further illustrate these effects, we present in Fig. 9(a–f) the results of two simulations where the head-on collision of the beam electrons with a 10^{23} W cm^{-2} laser plane wave is described using either a deterministic (continuous) model of (quantum-corrected) classical radiation reaction [53] (left column) or a Monte Carlo model of quantum synchrotron emission [45] (right column). The $x - y$ spatial distribution of the beam electrons following the interaction is displayed in Figs. 9(a,b). While the electron beam still appears to be well collimated in the classical radiation regime [Fig. 9(a)], it ends up being entirely scattered (in both forward and lateral directions) in the quantum radiation regime [Fig. 9(b)]. The $p_x - p_y$ momentum distribution of the beam electrons is shown in Figs. 9(c,d) during the interaction (at the time of maximal

angular divergence). In both classical and quantum regimes, the oscillating motion of the electrons in the laser field gives rise to a bow-shaped structure. In the classical regime, the electrons are quite uniformly distributed along this structure, which extends over $p_x/m_e c \sim \pm 100$ and $p_y/m_e c \sim \pm 200$. After the interaction [Fig. 9(c)], however, the beam electrons have recovered their initial small dispersion in p_y; thus, they present mostly longitudinal (positive) momenta with a reduced dispersion compared to their initial distribution, in accord with the well-known cooling effect of classical radiation friction [40]. In the quantum regime, the bowed momentum structure formed during the laser interaction [Fig. 9(d)] extends in p_y similarly to the classical case, but is shifted and broadened towards lower p_x ($-450 \lesssim p_x \lesssim 50$). Yet, in contrast to the classical case, most of the beam electrons are now concentrated at the bow head, in a region centered about $p_x/m_e c \sim 50$ and extending up to $p_x/m_e c \sim 450$ and $p_y/m_e c \sim \pm 100$. After the interaction [Fig. 9(f)], this cluster remains essentially unchanged, while there is only a faint trace of the bowed structure (which contains all the backscattered electrons, up to $p_x/m_e c \sim -450$). The large residual p_y-dispersion of the beam accounts for the strong spatial broadening observed in Fig. 9(b).

Another source of angular spread for the beam electrons is the transverse ponderomotive force associated with the small laser spot size. Contrary to the quantum photon emission, which increases the transverse particle momentum
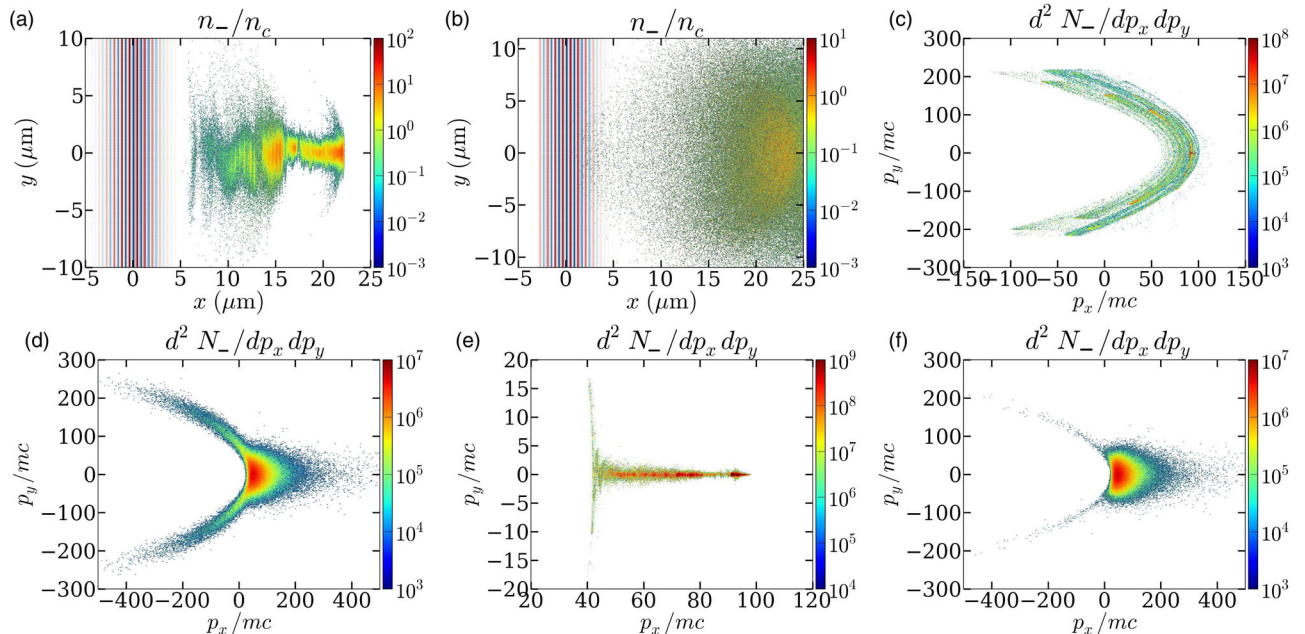

FIG. 9.   Laser-induced scattering of the beam electrons as predicted using classical radiation reaction (left column) or quantum synchrotron emission (right column). (a,b) Density distribution in the $x - y$ plane of the incoming beam electrons following the laser interaction. (c,d) Momentum distribution in the $p_x - p_y$ plane of the incoming beam electrons during the laser interaction at the time of maximum angular divergence. (e,f) Momentum distribution in the $p_x - p_y$ plane of the incoming beam electrons following the laser interaction. Note that the x-axis and the color map scales are changed in each figure.

only along the polarization y-axis, the ponderomotive force acts along both the y- and z-axes. The observed close variations of θ_{xy} and θ_{xz} during the interaction for both the positrons and electrons thus demonstrate that ponderomotive and QED effects become comparable under the present conditions (even though QED scattering still dominates for the positrons). One should note, however, that the important radiative deceleration in the longitudinal x-direction tends to amplify the ponderomotive-driven angular deflection.

In addition, we note that the electron-positron distribution resulting from the laser interaction is close but still not large or dense enough to sustain collective plasma effects since its typical size $\sim 2~\mu m$ turns out to be smaller than its skin depth $\sim 7~\mu m$ (assuming an electron-positron bunch of mean relativistic factor $\gamma_\pm = 200$ and density $n_\pm = 0.1 n_c$).

C. Influence of the laser parameters

We now examine how the laser parameters affect the positron production. To this goal, we have performed four laser-electron collision simulations with the same laser duration and energy as above but with various spot sizes: $d = 2, 3, 4$, and $5~\mu m$. The corresponding peak intensities are $I_0 = 10^{23}$, 4.4×10^{22}, 2.5×10^{22}, and $1.6 \times 10^{22}~W\,cm^{-2}$. To further assess the influence of the transverse field gradients, this set of simulations is supplemented with four other simulations employing a laser plane wave at intensities $I_0 = 10^{23}$, 5×10^{22}, 2.5×10^{22}, and $1.25 \times 10^{22}~W\,cm^{-2}$.

Figure 10(a) shows that, in our range of intensities, the production of γ-rays (of energies $> 2m_e c^2$) increases relatively slowly with the laser intensity for both planar and focused laser waves. The γ-ray yield for a plane wave is larger, and increases faster than for a focused wave since electrons have no chance to escape the laser field. This difference rises when shrinking the spot size due to fewer and fewer electrons traveling through the strong-field region. For a plane wave in the considered intensity range, the total number of emitted γ-rays (regardless of their subsequent decay into pairs) scales approximately as $N_\gamma^0 \sim 6 \times 10^{10} I_{22} + 1.56 \times 10^{11}$ (where I_{22} is the laser intensity in units of $10^{22}~W\,cm^{-2}$). Also, we have found that the corresponding high-energy (> 100 MeV) photon yield (not shown) weakly increases (from $\sim 4 \times 10^{10}$ to 7×10^{10}), tending to saturate when I_0 approaches $10^{23}~W\,cm^{-2}$. This is due to the strong γ-ray emission occurring in the foot of high-intensity pulses, which leads to important electron deceleration before the time of peak intensity, and therefore to the production of relatively low-energy photons on average. At lower intensities, radiative losses are diminished so that γ-ray emission takes place throughout the pulse duration at $I_0 = 1.25 \times 10^{22}~W\,cm^{-2}$. The weak sensitivity of the high-energy photon yield to the laser spot size/intensity is demonstrated by the similarity of the photon energy spectra plotted in Fig. 11(a). Higher intensities, however, augment the probability for moderate-energy (< 100 MeV) photons to be emitted.
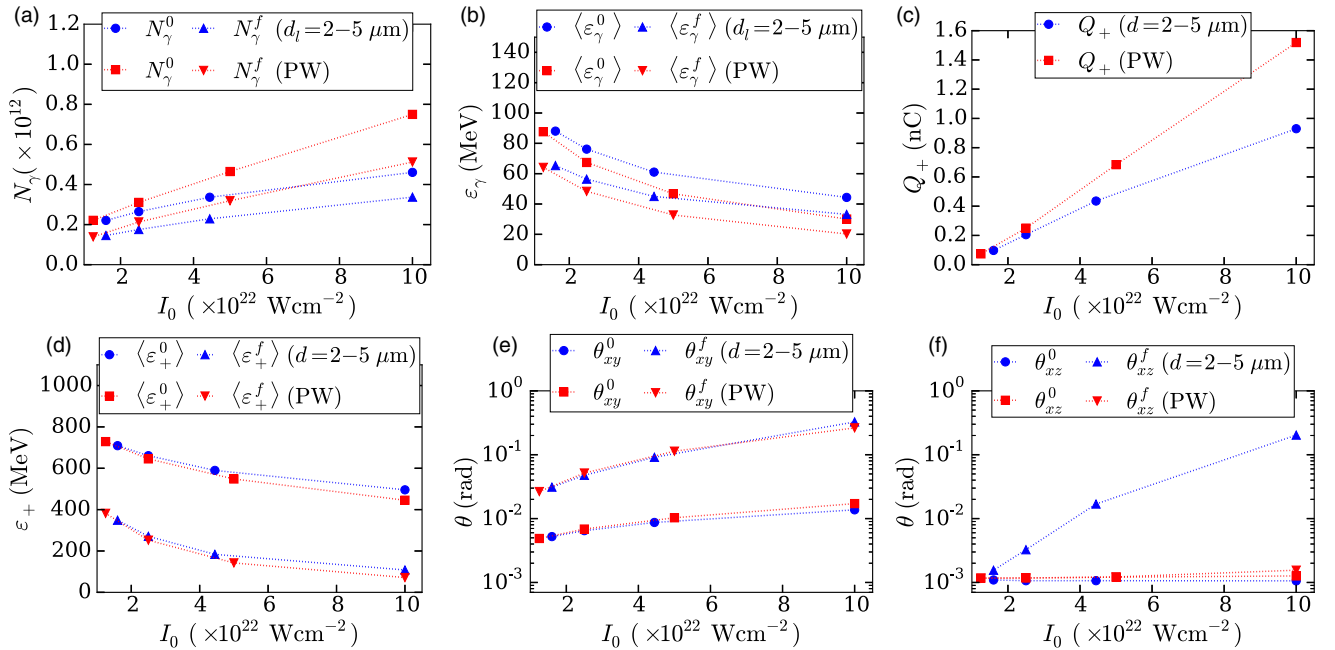

FIG. 10.   Laser intensity dependence of the total number of γ-rays (of energies $> 2m_e c^2$), N_γ (a), average γ-ray energy, $\langle \varepsilon_\gamma \rangle$ (b), total positron charge Q_+ (c), average positron energy, $\langle \varepsilon_+ \rangle$ (d), angular spread in the polarization plane, θ_{xy} (e), and in the perpendicular plane, θ_{xz} (e). The superscripts ^{0} and ^{f} denote quantities measured at creation time and at the end of the interaction, respectively, while the blue and red markers correspond to focused laser waves (of various spot sizes) and planar waves (PW).
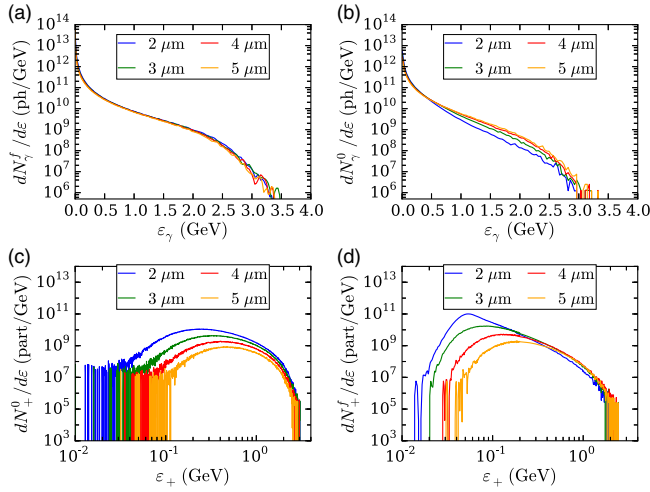
FIG. 11.   (a,b) Photon energy distributions (in photons per GeV) at creation time, $dN_\gamma^0/d\varepsilon$ (a) and at the end of the interaction, $dN_\gamma^f/d\varepsilon$ (b), for various laser spot sizes (or, equivalently, intensities). (c,d) Positron energy distributions (in particles per GeV) at creation time, $dN_+^0/d\varepsilon$ (c) and at the end of the interaction, $dN_+^f/d\varepsilon$ (d), for various spot sizes.

Consequently, as shown in Fig. 10(b), the average energy of the γ-ray photons (> 1 MeV) at creation time, $\langle \varepsilon_\gamma^0 \rangle$, drops with the laser intensity.

Figure 10(c) plots the total positron charge as a function of the laser intensity/spot size. In the plane-wave case, the positron charge is found to grow linearly as $Q_+[\text{nC}] \sim 0.17 I_{22} - 0.15$ in the range $1.25 \times 10^{22} \leq I_0 \leq 10^{23}$ W cm^{-2}). In the focused case, the total positron charge rises with the laser intensity, albeit at an increasingly slower rate. As for the photon emission, this behavior originates from the dropping number of electrons experiencing a strong field when the spot size is reduced, as well as from the strengthened transverse ponderomotive force that pushes the electrons sideways. When raising the laser intensity, the probability for lower-energy photons to decay into pairs is increased, which tends to boost the positron yield. This can be observed by comparing the final photon energy spectra obtained at various intensities/spot sizes [Fig. 11(b)]. At $I_0 = 10^{23}$ W cm^{-2} ($d = 2$ μm), the number of photons above 500 MeV that have been converted into pairs is significantly higher than at lower intensities. For all cases, the overall decrease in the high-energy photon number resulting from pair creation leads to a final average photon energy, $\langle \varepsilon_\gamma^f \rangle$, significantly reduced (by $\sim 20-30\%$) compared with $\langle \varepsilon_\gamma^0 \rangle$ [see Fig. 10(b)].

As the intensity rises, the low-energy γ-rays can more easily decay into pairs, thus enhancing the number of low-energy positrons. This is clearly shown by the positron energy spectra at creation time plotted in Fig. 11(c). Consequently, the average positron energy at birth is found to drop with the laser intensity as $\langle \varepsilon_+^0 \rangle[\text{MeV}] \sim 780 I_{22}^{-0.24}$ for both the focused and plane waves in the studied intensity

range [see Fig. 10(d)]. Moreover, during their subsequent interaction with the laser field, the positrons radiate a larger fraction of their energy at higher intensities: from $\sim 48\%$ at 1.25×10^{22} W cm^{-2} to 84% at 10^{23} W cm^{-2} for a plane wave. These stronger radiation losses explain the final positron energy spectra displayed in Fig. 11(d): quite unexpectedly, the number of high-energy γ-ray photons is the lowest at $I_0 = 10^{23}$ W cm^{-2} despite a higher yield at creation time [compare Figs. 11(a) and 11(b)]. This radiative effect further contributes to the decrease in the final mean positron energy, $\langle \varepsilon_+^f \rangle$, with laser intensity observed in 10(d). In the intensity range under consideration, we find that $\langle \varepsilon_+^f \rangle[\text{MeV}] \sim 490 I_{22}^{-0.8}$ for both the focused and plane waves. It appears that there exists an optimum laser intensity for maximizing the number of positrons above a given threshold energy. For instance, to get the maximal number of positrons beyond 100 MeV, the intensity $I_0 = 2.5 \times 10^{22}$ W cm^{-2} ($d = 4$ μm for a focused laser) gives the best results.

The intensity dependence of the positron angular spread in the polarization (xy) and perpendicular (xz) planes is depicted in Figs. 10(e,f). In the polarization plane, the angular spreads in the focused and plane-wave configurations present a similar increase with intensity (from $\theta_{+,xy}^f \sim 0.025$ rad at $I_0 = 1.5 \times 10^{22}$ W cm^{-2} to ~ 0.3 rad at $I_0 = 10^{23}$ W cm^{-2}), which confirms that QED scattering prevails in the considered intensity range. Also, both configurations entail a similar rise in the positron divergence during the interaction (from $\theta_{+,xy}^0$ to $\theta_{+,xy}^f$). In the perpendicular plane, the positron divergence mostly stems from the transverse ponderomotive force. As a result, for a laser plane wave, the final angular spread, $\theta_{+,xz}^f$, stays close to the initial value, $\theta_{+,xz}^0$. By contrast, $\theta_{+,xz}^f$ increases with narrowing focal spot and increasing intensity, up to a value close to $\theta_{+,xy}^f$ at $I_0 = 10^{23}$ W cm^{-2}.

In order to estimate the normalized transverse emittance of the pair distribution, $\epsilon_{n,\perp}$, we use the following approximation [54]:

$$\epsilon_{n,\perp} = \langle \gamma_+ \rangle \langle \beta_{+,x} \rangle \sigma_\perp \langle \theta_x \rangle \tag{3}$$

where $\langle \beta_{+,x} \rangle \sim 1$ is the average longitudinal velocity (normalized by c) of the pairs, $\sigma_\perp$ their RMS transverse width and $\langle \theta_x \rangle$ their RMS angular spread. In the intensity range $1.6 \times 10^{22} \leq I_0 \leq 10^{23}$ W cm^{-2}, the emittance is found to vary between $\epsilon_{n,\perp} = 0.1$ mm mrad and 0.07 mm mrad, the latter minimum value being obtained at $I_0 = 4.5 \times 10^{22}$ W cm^{-2}.

D. Noncollinear geometry

A noncollinear collision geometry ($\theta \neq 180°$) is generally used in experiments to prevent the reflected light from damaging the optics. For a focused laser, a larger fraction of the beam can effectively interact with the laser depending

of the collision angle, the spot size, and the beam size. As a preliminary investigation of the sensitivity of pair production to the collision angle, we have performed three simulations with incidence angles $\theta = 170°$, $150°$, and $90°$ (with $\varphi = 0$). All of the simulations consider a laser focused on the electron beam head, with a 3-μm spot size and a 4.4×10^{22} W cm^{-2} peak intensity. These simulations show that the total positron charge remains approximately unchanged ($Q_+ \approx 0.4$ nC) when the collision angle varies from $\theta = 180°$ to $150°$, in agreement with the predictions of the reduced kinetic-QED model [Fig. 2(c)]. In the worst-case perpendicular collision ($\theta = 90°$), the positron yield drops down to $Q_+ = 0.03$ nC, which amounts to $\sim 7\%$ of the yield in the reference collinear geometry. This value is also consistent with that ($\sim 10\%$) obtained with the reduced kinetic model despite the assumption of a laser plane wave.

IV. CONCLUSIONS

In summary, using full-scale 3D PIC simulations, we have demonstrated that soon-to-be-operational, multi-PW, multibeam lasers will enable all-optical, high-repetition-rate schemes for efficient pair creation via the multiphoton Breit-Wheeler process, which was, as yet, only accessible to large-scale accelerators. Besides providing a fully self-consistent modeling of the problem, our work presents important guidelines for future experiments. Our study thus reveals that the positron yield and mean divergence (resp. mean energy) increase (resp. decreases) with rising laser intensity at fixed laser energy. In particular, we find that a high-energy (~ 400 MeV), low-divergence (~ 0.02 rad) positron bunch of charge ~ 0.05 nC can be achieved using a moderately-intense ($\sim 10^{22}$ W cm^{-2}) laser pulse focused to a ~ 5-μm spot. Once magnetically segregated from the electrons, this beam could serve as an injector source in conventional or optical accelerators. Higher pulse intensities ($\sim 10^{23}$ W cm^{-2}) are required for generating dense ($Q_+ \sim 1$ nC, $n_+ \sim n_c$), quasineutral pair beams, at the expense, however, of an increased divergence ($\gtrsim 0.1$ rad) and a reduced mean energy (~ 100 MeV). Finally, we note that the electron-positron distributions obtained in our interaction conditions are not large or dense enough to sustain collective plasma effects since their typical size turns out to be smaller than their skin depth.

ACKNOWLEDGMENTS

[1] R. Ruffini, G. Vereshchagin, and S.-S. Xue, Electron-positron pairs in physics and astrophysics: From heavy nuclei to black holes, Phys. Rep. **487,** 1 (2010).

[2] S. Corde et al., Multi-gigaelectronvolt acceleration of positrons in a self-loaded plasma wakefield, Nature (London) **524,** 442 (2015).

[3] F. Tuomisto and I. Makkonen, Defect identification in semiconductors with positron annihilation: Experiment and theory, Rev. Mod. Phys. **85,** 1583 (2013).

[4] P. Mészáros, Theories of gamma-ray bursts, Annu. Rev. Astron. Astrophys. **40,** 137 (2002).

[5] A. M. Bykov and R. A. Treumann, Fundamentals of collisionless shocks for astrophysical application, 2. Relativistic shocks, Astron. Astrophys. Rev. **19,** 42 (2011).

[6] H. Chen, S. C. Wilks, J. D. Bonlie, E. P. Liang, J. Myatt, D. F. Price, D. D. Meyerhofer, and P. Beiersdorfer, Relativistic Positron Creation Using Ultraintense Short Pulse Lasers, Phys. Rev. Lett. **102,** 105001 (2009); H. Chen, F. Fiuza, A. Link, A. Hazi, M. Hill, D. Hoarty, S. James, S. Kerr, D. D. Meyerhofer, J. Myatt, J. Park, Y. Sentoku, and G. J. Williams, Scaling the Yield of Laser-Driven Electron-Positron Jets to Laboratory Astrophysical Applications, Phys. Rev. Lett. **114,** 215001 (2015).

[7] G. Sarri et al., Generation of a neutral, high-density electron-positron plasma in the laboratory, Nat. Commun. **6,** 6747 (2015).

[8] B. Shen and J. Meyer-ter Vehn, Pair and γ-photon production from a thin foil confined by two laser pulses, Phys. Rev. E **65,** 016405 (2001).

[9] A. R. Bell and J. G. Kirk, Possibility of Prolific Pair Production with High-Power Lasers, Phys. Rev. Lett. **101,** 200403 (2008).

[10] E. N. Nerush, I. Yu. Kostyukov, A. M. Fedotov, N. B. Narozhny, N. V. Elkina, and H. Ruhl, Laser Field Absorption in Self-Generated Electron-Positron Pair Plasma, Phys. Rev. Lett. **106,** 035001 (2011).

[11] O. J. Pike, F. Mackenroth, E. G. Hill, and S. J. Rose, A photon-photon collider in a vacuum hohlraum, Nat. Photonics **8,** 434 (2014).

[12] M. Lobet, C. Ruyer, A. Debayle, E. d'Humières, M. Grech, M. Lemoine, and L. Gremillet, Ultrafast Synchrotron-Enhanced Thermalization of Laser-Driven Colliding Pair Plasmas, Phys. Rev. Lett. **115,** 215003 (2015).

[13] H. Bethe and W. Heitler, On the stopping of fast particles and on the creation of positive electrons, Proc. R. Soc. A **146,** 83 (1934).

[14] H. J. Bhabha, The creation of electron pairs by fast charged particles, Proc. R. Soc. A **152,** 559 (1935).

[15] D. A. Gryaznykh, Y. Z. Kandiev, and V. A. Lykov, Estimates of electron-positron pair production in the interaction of high-power laser radiation with high-Z targets, JETP Lett. **67,** 257 (1998).

[16] CILEX Centre Interdisciplinaire Lumière Extrême. http://cilexsaclay.fr.

[17] ELI Extreme Light Infrastructure. http://www.eli-beams.eu.

[18] A. Di Piazza, C. Müller, K. Z. Hatsagortsyan, and C. H. Keitel, Extremely high-intensity laser interactions with fundamental quantum systems, Rev. Mod. Phys. **84,** 1177 (2012).

[19] T. Erber, High-energy electromagnetic conversion processes in intense magnetic fields, Rev. Mod. Phys. **38,** 626 (1966).

[20] A. I. Nikishov and V. I. Ritus, Pair production by a photon and photon emission by an electron in the field of an intense electromagnetic wave and in a constant field, JETP **25,** 1135 (1967).

[21] C. P. Ridgers, C. S. Brady, R. Duclous, J. G. Kirk, K. Bennett, T. D. Arber, A. P. L. Robinson, and A. R. Bell, Dense Electron-Positron Plasmas and Ultraintense γ Rays from Laser-Irradiated Solids, Phys. Rev. Lett. **108,** 165006 (2012).

[22] X.-L. Zhu, T.-P. Yu, Z.-M. Sheng, Y. Yin, I. C. E. Turcu, and A. Pukhov, Dense GeV electron–positron pairs generated by lasers in near-critical-density plasmas, Nat. Commun. **7,** 13686 (2016).

[23] C. S. Brady, C. P. Ridgers, T. D. Arber, A. R. Bell, and J. G. Kirk, Laser Absorption in Relativistically Underdense Plasmas by Synchrotron Radiation, Phys. Rev. Lett. **109,** 245006 (2012).

[24] N. B. Narozhny, S. S. Bulanov, V. D. Mur, and V. S. Popov, On e^+e^- pair production by colliding electromagnetic pulses, J. Exp. Theor. Phys. Lett. **80,** 382 (2004).

[25] S. S. Bulanov, T. Zh. Esirkepov, A. G. R. Thomas, J. K. Koga, and S. V. Bulanov, Schwinger Limit Attainability with Extreme Power Lasers, Phys. Rev. Lett. **105,** 220407 (2010).

[26] Y.-B. Wu and S.-S. Xue, Nonlinear Breit-Wheeler process in the collision of a photon with two plane waves, Phys. Rev. D **90,** 013009 (2014).

[27] S. V. Bulanov, T. Zh. Esirkepov, Y. Hayashi, M. Kando, H. Kiriyama, J. K. Koga, K. Kondo, H. Kotaki, A. S. Pirozhkov, S. S. Bulanov *et al.*, On the design of experiments for the study of extreme field limits in the interaction of laser with ultrarelativistic electron beam, Nucl. Instrum. Methods Phys. Res., Sect. A **660,** 31 (2011).

[28] K. Krajewska and J. Z. Kamiński, Breit-wheeler process in intense short laser pulses, Phys. Rev. A **86,** 052104 (2012).

[29] K. Krajewska and J. Z. Kamiński, Coherent combs of antimatter from nonlinear electron-positron-pair creation, Phys. Rev. A **90,** 052108 (2014).

[30] S. Meuren, C. H. Keitel, and A. Di Piazza, Semiclassical picture for electron-positron photoproduction in strong laser fields, Phys. Rev. D **93,** 085028 (2016).

[31] A. I. Titov, B. Kämpfer, A. Hosaka, T. Nousch, and D. Seipt, Determination of the carrier envelope phase for short, circularly polarized laser pulses, Phys. Rev. D **93,** 045010 (2016).

[32] M. J. A. Jansen and C. Müller, Strong-field breit-wheeler pair production in short laser pulses: Identifying multiphoton interference and carrier-envelope-phase effects, Phys. Rev. D **93,** 053011 (2016); M. J. A. Jansen, J. Z. Kamiński, K. Krajewska, and C. Müller, Strong-field breit-wheeler pair production in short laser pulses: Relevance of spin effects, Phys. Rev. D **94,** 013010 (2016); M. J. A. Jansen and C. Müller, Strong-field breit-wheeler pair production in two consecutive laser pulses with variable time delay, Phys. Lett. B **766,** 71 (2017).

[33] K. Tuchin, Non-linear pair production in scattering of photons on ultra-short laser pulses at high energy, Phys. Lett. B **686,** 29 (2010).

[34] I. V. Sokolov, N. M. Naumova, J. A. Nees, and G. A. Mourou, Pair Creation in QED-strong Pulsed Laser Fields Interacting with Electron Beams, Phys. Rev. Lett. **105,** 195005 (2010).

[35] S. S. Bulanov, C. B. Schroeder, E. Esarey, and W. P. Leemans, Electromagnetic cascade in high-energy electron, positron, and photon interactions with intense laser pulses, Phys. Rev. A **87,** 062110 (2013).

[36] D. L. Burke, R. C. Field, G. Horton-Smith, J. E. Spencer, D. Walz, S. C. Berridge, W. M. Bugg, K. Shmakov, A. W. Weidemann, C. Bula, K. T. McDonald, E. J. Prebys, C. Bamber, S. J. Boege, T. Koffas, T. Kotseroglou, A. C. Melissinos, D. D. Meyerhofer, D. A. Reis, and W. Ragg, Positron Production in Multiphoton Light-by-Light Scattering, Phys. Rev. Lett. **79,** 1626 (1997).

[37] A. Hartin, S. Porto, and G. Moortgat-Pick, Testing nonlinear-QED at the future linear collider with an intense laser, arXiv:1404.0810.

[38] G. Sarri, D. J. Corvan, W. Schumaker, J. M. Cole, A. Di Piazza, H. Ahmed, C. Harvey, C. H. Keitel, K. Krushelnick, S. P. D. Mangles *et al.*, Ultrahigh Brilliance Multi-MeV γ-ray Beams from Nonlinear Relativistic Thomson Scattering, Phys. Rev. Lett. **113,** 224801 (2014).

[39] F. Mackenroth and A. Di Piazza, Nonlinear Compton scattering in ultrashort laser pulses, Phys. Rev. A **83,** 032106 (2011).

[40] N. Neitz and A. Di Piazza, Stochasticity Effects in Quantum Radiation Reaction, Phys. Rev. Lett. **111,** 054802 (2013).

[41] M. Vranic, J. L. Martins, J. Vieira, R. A. Fonseca, and L. O. Silva, All-Optical Radiation Reaction at 10^{21} W/cm^2, Phys. Rev. Lett. **113,** 134801 (2014).

[42] T. G. Blackburn, C. P. Ridgers, J. G. Kirk, and A. R. Bell, Quantum Radiation Reaction in Laser-Electron-Beam Collisions, Phys. Rev. Lett. **112,** 015001 (2014); T. G. Blackburn, Measuring quantum radiation reaction in laser-electron-beam collisions, Plasma Phys. Controlled Fusion **57,** 075012 (2015).

[43] C. Harvey, M. Marklund, and E. Wallin, Relativistic Plasma Waves and Particle Beams as Coherent and Incoherent Radiation Sources, Proc. SPIE **9509,** 950908 (2015).

[44] N. V. Elkina, A. M. Fedotov, I. Yu. Kostyukov, M. V. Legkov, N. B. Narozhny, E. N. Nerush, and H. Ruhl, QED cascades induced by circularly polarized laser fields, Phys. Rev. ST Accel. Beams **14,** 054401 (2011).

[45] M. Lobet, E. d'Humières, M. Grech, C. Ruyer, X. Davoine, and L. Gremillet, Modeling of radiative and quantum electrodynamics effects in PIC simulations of ultra-relativistic laser-plasma interaction, J. Phys. Conf. Ser. **688,** 012058 (2016).

[46] J. G. Kirk, A. R. Bell, and I. Arka, Pair production in counter-propagating laser beams, Plasma Phys. Controlled Fusion **51**, 085008 (2009).

[47] W. Lu, M. Tzoufras, C. Joshi, F. S. Tsung, W. B. Mori, J. Vieira, R. A. Fonseca, and L. O. Silva, Generating multi-GeV electron bunches using single stage laser wakefield acceleration in a 3D nonlinear regime, Phys. Rev. ST Accel. Beams **10**, 061301 (2007).

[48] A. F. Lifschitz, X. Davoine, E. Lefebvre, J. Faure, C. Réchatin, and V. Malka, Particle-in-cell modelling of laser-plasma interaction using Fourier decomposition, J. Comp. Physiol. **228**, 1803 (2009).

[49] E. Lefebvre *et al.*, Electron and photon production from relativistic laser-plasma interactions, Nucl. Fusion **43**, 629 (2003).

[50] See Supplemental Material at http://link.aps.org/supplemental/10.1103/PhysRevAccelBeams.20.043401 for movies showing the evolution of the 3D density distribution of the photons, positrons and electrons during the laser interaction.

[51] H. Y. Wang, X. Q. Yan, and M. Zepf, Signatures of quantum radiation reaction in laser-electron-beam collisions, Phys. Plasmas **22**, 093103 (2015).

[52] S. R. Yoffe, Y. Kravets, A. Noble, and D. A. Jaroszynski, Longitudinal and transverse cooling of relativistic electron beams in intense laser pulses, New J. Phys. **17**, 053025 (2015).

[53] I. V. Sokolov, N. M. Naumova, J. A. Nees, G. A. Mourou, and V. P. Yanovsky, Dynamics of emitting electrons in strong laser fields, Phys. Plasmas **16**, 093115 (2009).

[54] S. Kneip, C. McGuffey, J. L. Martins, M. S. Bloom, V. Chvykov, F. Dollar, R. Fonseca, S. Jolly, G. Kalintchenko, K. Krushelnick, A. Maksimchuk, S. P. D. Mangles, Z. Najmudin, C. A. J. Palmer, K. Ta Phuoc, W. Schumaker, L. O. Silva, J. Vieira, V. Yanovsky, and A. G. R. Thomas, Characterization of transverse beam emittance of electrons from a laser-plasma wakefield accelerator in the bubble regime using betatron x-ray radiation, Phys. Rev. ST Accel. Beams **15**, 021302 (2012).